Revista Brasileira de Ensino de Física, vol. 47, e20240341 (2025)
www.scielo.br/rbef
DOI: https://doi.org/10.1590/1806-9126-RBEF-2024-0341

AERONET sun photometer as a didactic tool for understanding aerosol refractive index in the atmosphere: a case study for central Amazon

Marco A. Franco*[1], Pedro H.T. Tavares[2], Luciana V. Rizzo[2], Fernando G. Morais[2], Rafael Palácios[3], Paulo Artaxo[2,4]

[1]Universidade de São Paulo, Instituto de Astronomia, Geofísica e Ciências Atmosféricas, Departamento de Ciências Atmosféricas, São Paulo, SP, Brasil.
[2]Universidade de São Paulo, Instituto de Física, Departamento de Física Aplicada, São Paulo, SP, Brasil.
[3]Universidade Federal do Pará, Instituto de Geociências, Faculdade de Meteorologia, Belém, PA Brasil.
[4]Universidade de São Paulo, Centro de Estudos Amazônia Sustentável, São Paulo, SP, Brasil.

Received on September 13, 2024. Revised on December 21, 2024. Accepted on January 22, 2025.

As the impacts of climate change become increasingly evident, understanding the role of atmospheric aerosols in regulating Earth's climate is crucial. Despite their significance, the optical properties of aerosols remain unclear to the general public and, particularly, to students in Physical and Earth sciences. This paper presents a didactic approach to exploring variations in aerosol optical properties, focusing on refractive indices and utilizing data from the National Aeronautics and Space Administration's (NASA) AErosol RObotic NETwork (AERONET) under typical atmospheric conditions in central Amazon. The discussion presented here can be integrated into undergraduate and graduate university courses, linking Physics and environmental sciences and enhancing theoretical discussions in electromagnetism courses with observational data. The Amazon rainforest, with its dynamic atmospheric conditions influenced by seasonal changes, biomass-burning events, and long-range aerosol transport, provides a rich context for this analysis. Our study identifies seasonal patterns in aerosol optical depth, with biomass burning affecting light scattering at shorter wavelengths. African dust and smoke show strong absorption across a broader spectrum. We characterize the refractive index's wavelength-dependent behavior for the different aerosol conditions, highlighting their unique optical properties. This interdisciplinary analysis contributes to a deeper understanding of atmospheric sciences and its implications for climate modeling and environmental assessment.

Keywords: Atmospheric aerosols, refractive index, Amazon, AERONET, didactic approach.

1. Introduction

Optical atmospheric phenomena are pivotal for numerous scientific and environmental applications, ranging from weather prediction to climate modeling and air quality assessment [1, 2]. Among the atmospheric components, aerosols, defined as solid or liquid particles in suspension, are optically active in the visible range of the electromagnetic spectrum (400–700 nm). Most of the solar radiation reaching the Earth system is in the visible range, so the presence of aerosols leads to a variety of optical atmospheric phenomena, such as red sunset afterglow and haze. Atmospheric aerosols have size ranges from a few nanometers to tens of micrometers, being emitted by natural sources, like soil dust resuspension and biogenic emissions, and anthropogenic sources, such as fossil fuel and biomass combustion [1].

Atmospheric aerosols interact directly with solar radiation through scattering and absorption processes, diminishing the radiation reaching the Earth's surface [3]. That leads to a global cooling effect of about 0.5°C, counteracting part of the warming caused by the increase in greenhouse gas concentrations since the Industrial Revolution [4–6]. Aerosols also indirectly affect climate, influencing cloud microphysical properties and their ability to scatter sunlight and precipitate [7]. Therefore, aerosols are critical in regulating the Earth's radiative balance.

However, aerosols also pose significant risks to human health, contributing to respiratory and cardiovascular diseases [8]. To mitigate these health impacts, stricter air quality regulations have been adopted worldwide, targeting a reduction in aerosol emissions [9]. This creates a complex dilemma: reducing aerosols improves public health but removes their cooling effect, potentially leading to a more rapid increase in global temperatures and precipitation rates by 2100 [10]. From a broader perspective, this trade-off underscores the importance of integrated climate and air quality policies. Solutions must balance the dual goals of improving

---

*Correspondence email address: marco.franco@usp.br health outcomes and addressing climate change [11]. For example, transitioning to cleaner energy sources and adopting technologies that reduce both greenhouse gas and aerosol emissions can mitigate global warming without exacerbating health risks [12, 13]. Such strategies have the potential to ensure that the reduction in aerosols does not disproportionately accelerate warming, highlighting the necessity of addressing the root causes of both greenhouse gas emissions and aerosol pollution.

Aerosol optical properties are determined by their physical and chemical characteristics, like particle size distribution, morphology, and chemical composition. The latter determines the aerosol refractive index, which is an intensive property. Even though the aerosol-radiation interaction depends on many other attributes of the particles, such as its size and geometry, the real component of the refractive index provides insights into radiation scattering, while the imaginary component informs about radiation absorption, both exhibiting wavelength (λ) dependency [3, 14]. In turn, the aerosol chemical composition depends on the characteristics of emission sources and atmospheric processes.

The study of atmospheric aerosols, particularly concerning their physical properties, has a long and rich history tracing back to pioneering work by scientists in the 19th century [15–17]. Early investigations, such as the theoretical studies by Lord Rayleigh in the 1870s and Lorenz in the 1890s on light scattering, laid the groundwork for understanding the interactions between light and small and larger particles [18, 19]. By the early 20th century, Ångström's work, together with the development of the Mie theory for particles with sizes of the order of the radiation wavelength, introduced mathematical models to quantify the wavelength dependency of aerosol scattering, forming an essential basis for modern aerosol science [20–22]. However, these studies were limited by the available technology, relying on rudimentary optical instruments and manual observations to infer aerosol properties from atmospheric phenomena like haze and red sunsets.

Throughout the 20th century, technological advances transformed how aerosols were understood and their properties measured. At the beginning of the century, the first nephelometers and relatively modern sun photometers were introduced, providing an initial method for assessing the optical properties of aerosols [17]. The first photometers measured solar radiation's attenuation at specific wavelengths as it passed through the atmosphere [23, 24]. Typically, they consisted of a photosensitive element, such as a photodiode or photoresistor, combined with filters to isolate specific wavelengths of sunlight. The data collected required manual recording and interpretation, and although innovative for their time, these instruments lacked the precision and standardization needed for large-scale or comparative studies.

The 1980s marked a revolutionary shift with the advent of automated and digital sun photometers for measuring atmospheric aerosols. A major milestone was the establishment of National Aeronautics and Space Administration's (NASA) AErosol RObotic NETwork (AERONET), a global collaborative network that standardized automated and calibrated sun photometers to ensure high-quality data [25–27]. These instruments enabled precise measurements of aerosol optical depth (AOD), refractive indices, and other critical radiative properties, facilitating comparative studies on a global scale. AERONET provided significant advancements by offering consistent data under various environmental conditions, becoming a cornerstone for climate and atmospheric research.

Given the relevance of aerosols to the Earth's radiative balance, climate, and air quality, it is essential to educate the public, especially young scientists, about aerosol properties and environmental impacts. This study proposes a didactic approach utilizing data from NASA's AERONET network to examine, among other optical properties, the refractive index variation due to the presence of atmospheric aerosols under typical atmospheric conditions in the central Amazon. We aim to augment theoretical frameworks discussed in electromagnetism undergraduate and graduate courses with empirical data. The Amazon rainforest was selected as the focus of this study due to its dynamic atmospheric conditions influenced by seasonal variations, biomass-burning events, interactions with adjacent regions, and long-range transport of aerosols and smoke [28–31]. This mixture of aerosol compositions and distributions offers a rich opportunity to evaluate the differences in the refractive indices. The pristine Amazonian atmosphere, which is typically very clean, serves as a baseline for comparison, allowing us to assess the impact of external aerosol sources on their optical properties.

Specifically, we examine AERONET data collected in atmospheric conditions characterized by natural Amazonian aerosols, regional biomass-burning events, and African dust and smoke advection. By incorporating AERONET data into discussions on refractive indices, we strive to enhance the pedagogical effectiveness of physics and environmental education. This approach offers students practical insights into complex scientific concepts and opens new possibilities for interdisciplinary didactic methods, thus bridging the gap between theoretical knowledge and real-world applications.

2. Theoretical Framework

The refractive index, defined here as $\mathrm{m} = \mathrm{n} + i\mathrm{k}$ (following the literature [1]), is a complex number governing the behavior of electromagnetic radiation as it propagates through different mediums [14], including the atmosphere [32]. Its significance lies in its ability to dictate the deviation of light rays, influencing how they are scattered or absorbed when transitioning between different mediums. At a given wavelength, the refractive index's real part, n, is defined as the ratio between the light speed in the medium and in the vacuum. In contrast, the imaginary part, k, describes the absorption properties of the medium [14]. Atmospheric gases and aerosols exhibit absorption and scattering properties that depend on their composition and physical properties [1, 32].

When electromagnetic radiation interacts with atmospheric components, certain wavelengths can be absorbed or scattered, reducing the radiation's intensity reaching the Earth's surface. The scattering of electromagnetic radiation by aerosols, in particular, depends on the size of the particles relative to the wavelength of the incident radiation. This interaction falls into two primary scattering regimes: Rayleigh scattering and Mie scattering [32]. Rayleigh scattering occurs when particles are much smaller than the wavelength of the radiation ($radius \ll \lambda$), leading to a strong wavelength dependence where shorter wavelengths are scattered more efficiently. This mechanism is responsible for phenomena such as the blue color of the sky. In contrast, Mie scattering becomes significant when particle sizes are comparable to the wavelength of the radiation ($radius \sim \lambda$).

The Mie theory describes most aerosols' optical properties, which explains how light interacts with particles of this size range. According to this theory, aerosol optical properties are determined by two key parameters: the refractive index, m, and the size parameter ($x = 2\pi r/\lambda$). The size parameter x is critical for identifying the scattering regime. When x is much less than 1, the particle is significantly smaller than the wavelength, resulting in Rayleigh scattering. When x is approximately 1, the particle size is comparable to the wavelength, leading to Mie scattering, characterized by more complex scattering patterns in both forward and backward directions. For x much greater than 1, the particle is much larger than the wavelength, and scattering approximates geometric optics, with light predominantly scattered in the forward direction. For more details, the reader is referred to [33].

Different materials have distinct refractive indices, which determine their ability to absorb and scatter radiation at specific wavelengths. For example, gases such as ozone (O_3), nitrogen oxides (NO_x), carbon dioxide (CO_2), methane (CH_4), and water vapor have absorption bands in the ultraviolet (UV) and/or infrared (IR) regions of the electromagnetic spectrum [1]. In the visible and near-infrared ranges, atmospheric aerosols may absorb radiation, notably through components such as black and brown carbon [34, 35], and scatter radiation, as seen in sulfate aerosols [32]. The aerosol absorption and scattering efficiencies depend strongly on particle size distribution and chemical composition. In turn, aerosol physical and chemical properties are very dynamic, depending on the characteristics of emission sources and atmospheric processes like size-selective particle removal and chemical reactions. Consequently, aerosol optical properties vary in space and time, and this variability can be used to infer the influence of different emission sources and atmospheric processes [32].

2.1. Mathematical formulation of the refractive index of atmospheric aerosols

The refractive index is intrinsically linked to the properties of the medium, such as permittivity and permeability [14]. Those quantities, in turn, depend on the constituents of the medium. For a general and didactic discussion on the refractive index of atmospheric aerosols, it is typically sufficient to consider the following approximations:

1. The magnetic field can be neglected [36];
2. The atmosphere can be modeled as a dielectric medium [2] composed solely of dry air and diluted atmospheric aerosols with a concentration of about tens of μg/m^3 [1, 37].

The first consideration is verified as most aerosols encountered in typical atmospheric conditions demonstrate minimal magnetic behavior [36], rendering the electric field the primary focus for the subsequent analysis. Furthermore, the second approximation is supported by the capacity of AERONET sun photometers and their retrieval algorithms to discern water vapor from aerosol radiative effects effectively. Therefore, although the density of water vapor, which strongly depends on the latitude and longitude [2], is typically found in the atmosphere at orders of magnitudes of about a few g/m^3, it does not impact the following analysis. In addition, AERONET retrievals also discount the absorption contributions of O_3, NO_x, CO_2, and CH_4 [38]. An atmosphere composed exclusively of dry air at $\lambda = 589$ nm has a refractive index of m $= 1.00029 + 0i$ [1]. For different wavelengths, ranging from 250 nm to 1690 nm, n for dry air varies very little, from 1.00031 to 1.00027 [39]. Thus, discounting the absorption contributions from gases, the dry air atmosphere is approximately transparent to solar radiation, so the interaction with radiation is mainly due to atmospheric aerosols. Therefore, we can focus solely on the electric field induced by the solar radiation in the atmospheric aerosols to derive the refractive index equation.

The following demonstration is didactically adapted to our considerations and based on widely used Physics course bibliography [14, 40, 41]. When solar radiation penetrates the atmosphere, it induces polarized charges in the constituents of the medium. This polarization phenomenon results in the displacement vector ($\mathbf{D}$) being expressed as a function of the electric field ($\mathbf{E}$) and the polarization ($\mathbf{P}$)

$$\begin{aligned}\mathbf{D} &= \varepsilon_0\mathbf{E} + \mathbf{P} = \varepsilon_0\mathbf{E} + \varepsilon_0\chi_e(\omega)\mathbf{E}\\ &= \varepsilon_0(1+\chi_e(\omega))\mathbf{E} = \varepsilon_0\varepsilon_r(\omega)\mathbf{E},\end{aligned} \tag{1}$$

where ε_0 represents the vacuum's permittivity, $\varepsilon_r(\omega)$ represents the effective permittivity, which is a function of the frequency (ω) of the incident radiation, and $\chi_e(\omega)$ is the electric susceptibility. The polarization, in general, does not oscillate in phase with the electric field, implying that $\chi_e(\omega)$ is a complex number and, therefore, $\varepsilon_r(\omega)$ is also a complex number, e.g., $\varepsilon_r(\omega) = \varepsilon_{r1}(\omega) + i\varepsilon_{r2}(\omega)$.

We now consider a monochromatic plane wave of the form

$$\mathbf{E}(\mathbf{r}, t) = \mathbf{E}_0 e^{i(\mathbf{k}\cdot\mathbf{r} - \omega t)}, \tag{2}$$

where $\mathbf{k}$ is the propagation vector.

Under the assumption of a dry atmosphere containing suspended aerosol particles, the atmosphere behaves like an insulator since these particles represent only a small fraction of the atmosphere in terms of volume and mass. Thus, treating the atmosphere as “source-free” simplifies Maxwell’s equations, aiding the study of electromagnetic fields on macroscopic scales without compromising accuracy. The macroscopic Maxwell’s equations for a source-free system are

$$\nabla\cdot\mathbf{D} = 0 \tag{3}$$

$$\nabla\cdot\mathbf{B} = 0 \tag{4}$$

$$\nabla\times\mathbf{E} = -\frac{\partial\mathbf{B}}{\partial t} \tag{5}$$

$$\nabla\times\mathbf{H} = \frac{\partial\mathbf{D}}{\partial t}. \tag{6}$$

For a wave like the one represented by Equation (2), the operators $\partial/\partial t$ and ∇ are expressed as

$$\frac{\partial\mathbf{E}}{\partial t} = -i\omega\mathbf{E},\ \nabla\cdot\mathbf{E} = i\mathbf{k}\cdot\mathbf{E} \tag{7}$$

Thus, the Maxwell’s equations in the atmosphere can be represented as

$$i\mathbf{k}\cdot\mathbf{D} = 0 \rightarrow\ i\varepsilon_0\varepsilon_r(\omega)\mathbf{k}\cdot\mathbf{E} = 0 \tag{8}$$

$$i\mathbf{k}\cdot\mathbf{B} = 0 \tag{9}$$

$$i\mathbf{k}\times\mathbf{E} = \frac{i\omega}{c}\mathbf{B} \tag{10}$$

$$i\mathbf{k}\times\mathbf{H} = -\frac{i\omega}{c}\mathbf{D} =\!\rightarrow i\mathbf{k}\times\frac{\mathbf{B}}{\mu} = -\frac{i\omega}{c}\varepsilon_0\varepsilon_r(\omega)\mathbf{E}, \tag{11}$$

where c is the speed of light in vacuum, defined as $c = 1/\sqrt{\mu_0\varepsilon_0}$; μ_0 is the vacuum’s permeability, and ε_0 is the vacuum’s permittivity.

From Equations (8) and (9), it is obtained that the electric and magnetic fields are perpendicular to $\mathbf{k}$. To get the dispersion relation for electromagnetic waves in the atmosphere, we apply ($\mathbf{k}\times$) in Equation (10) and using Equation (11), it is shown that

$$i\mathbf{k}\times(\mathbf{k}\times\mathbf{E}) = \frac{i\omega}{c}\mathbf{k}\times\mathbf{B} \tag{12}$$

$$i\mathbf{k}\times\mathbf{B} = \frac{-i\omega\mu\varepsilon_0\varepsilon_r(\omega)}{c}\mathbf{E} \tag{13}$$

$$\Rightarrow i\mathbf{k}\times(\mathbf{k}\times\mathbf{E}) = \frac{i\omega}{c}\left(\frac{-\omega\mu\varepsilon_0\varepsilon_r(\omega)}{c}\right)\mathbf{E}, \tag{14}$$

where here we applied the triple cross product property, $i\mathbf{k}\times(\mathbf{k}\times\mathbf{E}) = i[\mathbf{k}(\mathbf{k}\cdot\mathbf{E})] - i[\mathbf{k}\cdot\mathbf{k}(\mathbf{E})]$. From Equation (8), $\mathbf{k}\cdot\mathbf{E} = 0$, then

$$-ik^2\mathbf{E} = \frac{-i\omega^2}{c^2}\mu\varepsilon_0\varepsilon_r(\omega)\mathbf{E} \tag{15}$$

$$\Rightarrow k^2 = \frac{\omega^2}{c^2}\mu\varepsilon_0\varepsilon_r(\omega). \tag{16}$$

Equation (16) expresses the dispersion relation for waves in our modeled atmosphere (note that it is the same as for a dielectric medium). The wave velocity (v) depends on the frequency. Since the refractive index is defined as $\mathrm{m} = {}^{c}/_{\mathrm{v}}$ and $\mathrm{v} = {}^{\omega}/_{|\mathbf{k}|}$ then

$$\mathrm{m} = \sqrt{\mu\varepsilon_0\varepsilon_r(\omega)} = \sqrt{\mu\varepsilon_0(\varepsilon_{r1}(\omega) + i\varepsilon_{r2}(\omega))} \Leftrightarrow \mathrm{m}(\omega) = \mathrm{n}(\omega) + i\kappa(\omega). \tag{17}$$

Thus, m is a complex number dependent on the frequency, which directly implies that $\mathbf{k} = \mathbf{k}_1 + i\mathbf{k}_2$ is also a complex number. If we consider here a wave propagating in the $\hat{\mathbf{z}}$ direction, the wave represented by Equation (2) can be expressed as

$$\mathbf{E}(z, t) = \mathbf{E}_0 e^{i[(k_1 - ik_2)\cdot z - \omega t]} = \mathbf{E}_0 e^{-k_2 z} e^{i(k_1 z - \omega t)}. \tag{18}$$

Note that Equation (18) has two important components:

- The term $e^{-k_2 z}$ is associated with the imaginary refractive index and represents the attenuation of the radiation due to absorption from the atmospheric aerosols in the atmosphere. This component can also be interpreted as the transfer of energy from the electromagnetic wave into the aerosol particles;
- The term $e^{i(k_1 z - \omega t)}$ is associated with the real component of the refractive index and represents the wave oscillation through the atmosphere.

The presence of different aerosol populations in the atmosphere, with different chemical compositions, results in different interactions of the particles with the electromagnetic radiation, absorbing or scattering it. Also, this interaction depends directly on the wavelength since $\omega = \omega(\lambda)$. Thus, we exemplify these conditions and dependencies using AERONET data in the following sections.

3. Materials and Methods

The following sections outline the AERONET network, the Amazon Tall Tower Observatory (ATTO) site in central Amazon, and the selected periods for assessing various sources and their effects on the aerosol optical properties, particularly the real and imaginary components of the refractive index.

3.1. AERONET sun photometers

AERONET is a collaborative network of ground-based remote-sensing photometers established by NASA and maintained by worldwide partner scientists [25]. The network comprises solar and lunar spectroradiometers of the Cimel Electronic 318A and 318T models, subject to strict standardization of calibration and processing to ensure data quality. Although other networks like Pandora measure atmospheric properties with solar photometers, AERONET is the largest and best known for atmospheric aerosols.

Figure 1 shows the ATTO's sun photometer, installed at 80 m height. The AERONET available data is classified into three quality levels: 1.0, 1.5, and 2.0, which consist of all unscreened data, automatically cloud-cleared data, and manually inspected calibrated data, respectively [26]. This study considers daily average data level 1.5 between February 2016 and April 2024 obtained from the AERONET public domain repository, accessible at https://aeronet.gsfc.nasa.gov/.

The AERONET provides data on various physical properties of the atmospheric aerosols. Each sun photometer measures the irradiance received at ground level across different wavelengths at a given time. Retrieval algorithms calculate the AOD and the precipitable water vapor. The AOD is a measure of the radiation extinction at a particular wavelength due to aerosol-atmosphere interactions from the surface to the top of the atmosphere (TOA, defined as 100 km height [31]).

Figure 1: Cimel sun photometer from the AERONET network at the Amazon Tall Tower Observatory (ATTO) site.

The AOD is calculated as

$$\mathrm{AOD}(\lambda) = \int_{\mathrm{surface}}^{\mathrm{TOA}} \sigma_{\mathrm{ext},\lambda}(z)dz, \tag{19}$$

where $\sigma_{\mathrm{ext},\lambda}(z)$ is the extinction coefficient, which accounts for the scattering and absorption of radiation by atmospheric aerosols and is wavelength-dependent

$$\sigma_{\mathrm{ext}}(\lambda) = \sigma_{\mathrm{scat}}(\lambda) + \sigma_{\mathrm{abs}}(\lambda). \tag{20}$$

The AOD is an extensive property, which means that it depends on the particle number concentrations. In fact, higher aerosol loading results in greater radiation extinction and AOD values, respectively [28, 31]. Therefore, AOD infers the column aerosol loading in the atmosphere. The AERONET provides AOD data in several wavelengths. Considering the coincident products (e.g., when all the AERONET products were available simultaneously), wavelengths from the visible 440 nm to near-infrared 1020 nm were considered for the daily average data.

AERONET also provides data obtained through inversion algorithms, which refer to computational methods that retrieve or infer specific parameters or properties of interest from observed data [26, 38]. The AERONET inversion algorithms consider a sort of assumptions, such as those described in Section 2, to compensate for the absorption by different gases in the atmosphere. The algorithms also discriminate the aerosol geometry into spherical and non-spherical particles and their vertical distribution along a plane-parallel atmosphere with different surface refletances [38]. For detailed information on the inversion algorithms, the reader is referred to the AERONET documentation [42]. In this study, in addition to AOD, we use the following inversion products: refractive index (real and imaginary parts), absorption AOD (AAOD), the asymmetry factor (AF), the single scattering albedo (SSA), and aerosol volume distribution as a function of particle size. Unlike the AOD, the AAOD accounts only for the aerosol absorption effects, being a measure of the atmospheric column loading of light-absorbing particles such as black carbon and mineral dust. In addition, the aerosol particle size distribution is a key physical property, influencing the aerosol scattering efficiency under the Mie scattering regime [43].

The spectral dependency of both the AOD and AAOD is useful to infer the presence of different aerosol populations [28, 44]. The AOD (and the AAOD) typically decreases with wavelength as a power law function

$$\mathrm{AOD}(\lambda) = \beta\lambda^{-\alpha}, \tag{21}$$

where β is known as the turbidity coefficient and α is the Ångström exponent [3]. The α parameter is a widely used to describe the wavelength dependence of the AOD, as defined in Equation 21. The Ångström exponent is an intensive optical property, which means that it is independent of the quantity of aerosol present and instead reflects the size distribution and spectral dependency of aerosol particles. Typically, α is positive, indicating that AOD decreases with increasing wavelength, a behavior characteristic of fine-mode aerosols like smoke or pollution. However, a negative Ångström exponent is also possible and occurs under specific atmospheric conditions. A negative α suggests that AOD increases with wavelength, which is generally associated with the dominance of larger particles, such as coarse-mode aerosols (e.g., mineral dust or sea salt). This behavior arises because larger particles scatter light more efficiently at longer wavelengths than shorter ones, resulting in an inverse spectral dependency. This can also occur in mixed aerosol populations if the coarse-mode particles significantly outweigh the fine-mode particles in terms of optical contribution, effectively reversing the expected trend [1]. In general, it is considered that a larger α value indicates a stronger decrease in AOD with wavelength, suggesting dominance by fine-mode aerosols, while smaller values are indicative of coarse-mode particles such as dust.

Equation 21 can be viewed as a specific application of the Beer-Lambert-Bouguer law, which describes the attenuation of light intensity as it propagates through a medium. In atmospheric optics, the total optical depth, $\tau(\lambda)$, a key parameter in the Beer-Lambert-Bouguer law, is the sum of contributions from various atmospheric components. The AOD represents the contribution of aerosols to the total optical depth and thus encapsulates the aerosol-specific attenuation properties. The Beer-Lambert-Bouguer law is given by

$$I(\lambda) = I_0(\lambda) e^{-\tau(\lambda)}, \tag{22}$$

where $I(\lambda)$ is the transmitted intensity of light at wavelength λ, $I_0(\lambda)$ is the initial intensity, and $\tau(\lambda)$ is the total optical depth. In this context, AOD(λ) is a component of $\tau(\lambda)$ and is parameterized in Equation 21 to capture its spectral behavior due to aerosols. This wavelength dependence of the AOD expressed through α and β provides valuable insights into aerosol size distributions and compositions.

In this work, the scattering Ångström exponent (SAE) characterizes the wavelength dependence of aerosol scattering properties, providing insight into the aerosol size distribution and composition. SAE is derived from AERONET data as the exponent between 440 and 870 nm, using the following relation [32]

$$\mathrm{SAE} = -\frac{\ln\left(\frac{\mathrm{AOD}(\lambda_1)}{\mathrm{AOD}(\lambda_2)}\right)}{\ln\left(\frac{\lambda_1}{\lambda_2}\right)}, \tag{23}$$

where AOD(λ_1) and AOD(λ_2) are the aerosol optical depth values at wavelengths λ_1 and λ_2, respectively. This intensive optical property indicates how aerosol scattering efficiency varies with wavelength, with higher SAE values suggesting a larger proportion of fine-mode aerosols that scatter light more efficiently at shorter wavelengths. Additionally, the absorption Ångström exponent (AAE) was estimated analogously using the wavelength pair 440-880 nm, but with the AAOD instead of the AOD, to characterize the wavelength dependence of the aerosol absorption. AAE values help distinguish between different aerosol types based on their absorption properties, with higher values indicating a greater decrease in absorption efficiency with increasing wavelength.

Two other key intensive aerosol properties that are important for quantifying their radiative effects are the single scattering albedo, SSA, and the asymmetry factor, AF. The SSA is defined as the ratio of scattering to total extinction (scattering + absorption) by aerosol particles. It quantifies the relative importance of scattering versus absorption in the aerosol's interaction with light. SSA values range from 0 to 1, where a value close to 1 indicates that scattering dominates, while a value closer to 0 suggests strong absorption. This property is critical for determining whether aerosols contribute to cooling (scattering) or warming (absorption) of the atmosphere and is thus a key parameter in assessing their radiative forcing [32].

In addition, the asymmetry factor quantifies the directionality of radiation scattering by aerosol particles. It is defined as the average cosine of the scattering angle (θ), given by

$$\mathrm{AF} = \langle \cos\theta \rangle = \int_0^{2\pi} \int_0^{\pi} \cos(\theta) P(\theta) \sin(\theta)\, d\theta\, d\phi, \tag{24}$$

where $P(\theta)$ is the scattering phase function, representing the angular distribution of scattered light, and $\sin(\theta)$ accounts for the spherical geometry of the scattering process. The asymmetry factor ranges from -1 to 1. A positive AF indicates forward scattering, with values closer to 1 typical of larger particles that strongly scatter light in the forward direction. An AF near 0 signifies isotropic scattering, and negative values represent backward scattering. This parameter is critical for understanding how aerosols influence the angular distribution of solar radiation in the atmosphere and is a key input for radiative transfer models in climate studies [32].

It is worth mentioning that the AERONET network estimates the complex refractive index of aerosols through a simultaneous inversion of direct solar radiation and sky radiance measurements at multiple wavelengths [26]. This inversion retrieves the aerosol particle size distribution and the refractive index by fitting observed radiances to a theoretical model based on Mie scattering for homogeneous spherical particles. The refractive index can vary with wavelength, and smoothness constraints are applied to ensure a gradual spectral variation, thus improving the stability and accuracy of the retrieval. The process employs statistical

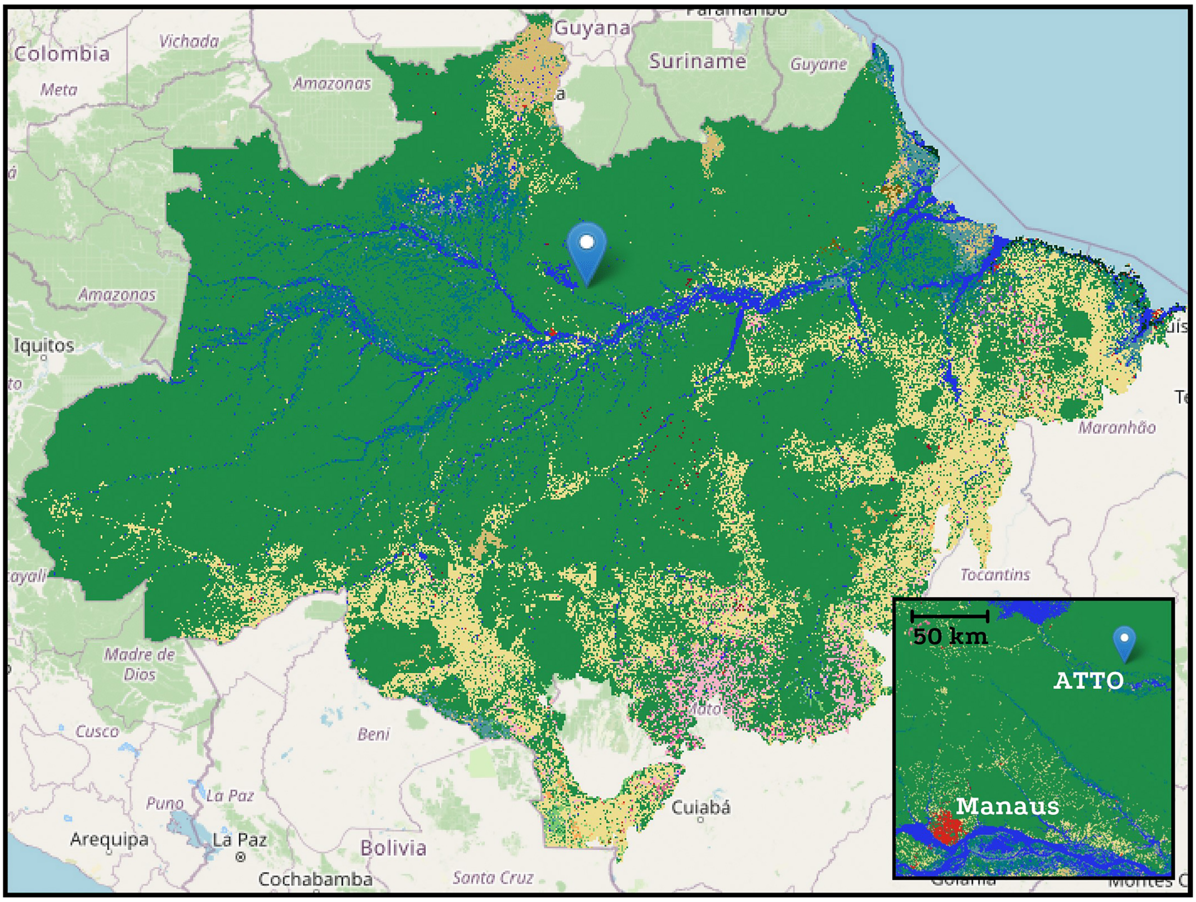

Figure 2: Geographic location of the Amazon Tall Tower Observatory (ATTO) site. The colors represent the land cover in the region, where, for example, green stands for forest, blue for water bodies, and the other colors for different coverage.

optimization techniques, accounting for different levels of measurement noise and uncertainties in the data. The retrieval algorithm adjusts the model iteratively, minimizing the difference between observed and simulated radiances while applying a priori constraints to the aerosol characteristics.

Although this study focuses solely on using the AERONET network to investigate the optical properties of atmospheric aerosols, it is important to acknowledge the availability of additional data sources that can complement and enhance future research. Remote sensing data products, such as those from MODIS (Moderate Resolution Imaging Spectroradiometer) [45] and MISR (Multi-angle Imaging Spectroradiometer) [46], provide valuable spatial coverage and can help identify regional and global patterns in fine-mode and coarse-mode aerosols. These datasets offer an opportunity for cross-validation with ground-based observations, strengthening the analysis of aerosol dynamics and providing a broader spatial context.

3.2. The ATTO site

The ATTO site is located in central Amazon, approximately 150 km northeast (upwind) of Manaus city [47]. Figure 2 shows the site's geographical location. The site was selected due to its privileged location, which enables the study of different atmospheric conditions due to the confluence of air masses throughout the year [48].

During the wet season, which spans from February to May, pristine conditions prevail at the site due to the strong rain showers [49], cleaning the atmosphere. Also, air masses crossing mostly untouched regions of the Amazon rainforest prevail during the wet season. When pristine conditions are observed, atmospheric aerosols, with an average number concentration of 280 cm^{-3} [50], are mostly emitted by biogenic sources, such as spores, fungi, soil dust, and bacteria, or produced in the atmosphere by the oxidation of volatile organic compounds [51–54]. Figure 3, obtained with scanning electron microscopy, shows aerosols collected during the wet season 2019 at the ATTO site using a polycarbonate filter. The particles present a spherical-like shape, which agrees with the literature for the region [55], and average sizes of about 100 to 500 nm.

In contrast, during the dry season, which spans from August to November, regional biomass burning dominates the atmospheric aerosols [28, 52], with average particle number concentrations of 1400 cm^{-3} [50]. Particularly, most of the atmospheric carbonaceous aerosols

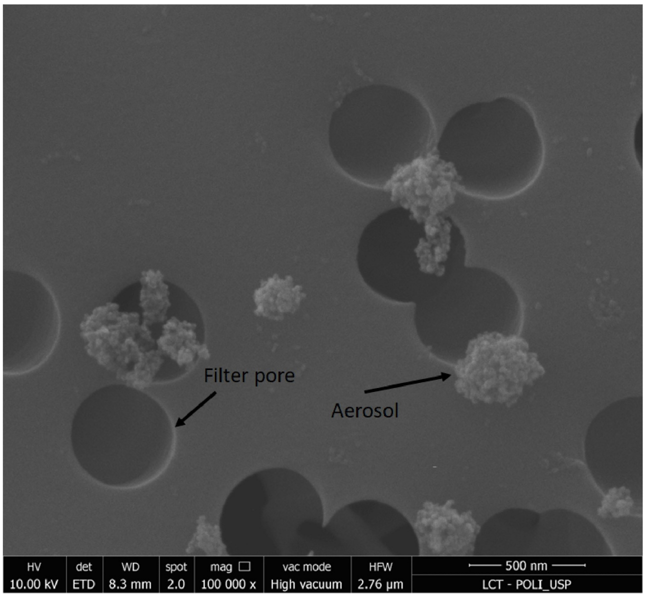

Figure 3: Aerosols sampled at the ATTO site, in central Amazon, with polycarbonate filters during the wet season of 2019. The image was obtained from scanning electron microscopy.

during this period are black carbon [44, 56], which strongly interacts with solar radiation, mainly in the near-infrared portion of the spectra [57]. During both wet and dry seasons, sporadic long-range transport events bring African dust and smoke to the Amazonian atmosphere [30, 58].

Recent studies have shown the influx of atmospheric smoke plumes from the African continent throughout the year and pointed out that it contributes to up to 30% of the black carbon fraction in the Amazonian dry season. In contrast, during the wet season, the fraction of black carbon due to African pollution may reach averages up to 60 % [30]. In particular, during the wet season, and due to the direction of the air masses, Saharan dust is transported from the African continent to South America, which impacts the aerosol population at the ATTO site strongly. Therefore, studying the different aerosol populations, with their particular chemical composition and mixture, is a rich opportunity to evaluate the variability of atmospheric refractive index in the atmosphere.

3.2.1. Selection of the atmospheric conditions

To exemplify the different aerosol influences in the refractive index discussed in Section 2, three different atmospheric conditions were selected. They illustrate the contributions of biogenic, regional biomass-burning, and African dust and smoke emissions on the real and imaginary parts of the refractive index. The considerations made here are based especially on the discrimination of the optical properties of aerosols presented in [30]. In addition, we use information from Ångström matrices to separate the different contributions of aerosols. The reader interested in deepening the knowledge about Ångström matrices can consult [59]. The criteria to identify the different atmospheric conditions was based on aerosol physical properties investigated in previous studies:

a. Pristine conditions: days with average AOD at 440 nm ≤ 0.1 [60, 61].
b. African dust and smoke conditions: days with average SAE and AAE satisfying the conditions: $1.0 \leq \text{AAE} \leq 1.5$ and $-1 \leq \text{SAE} \leq 1.5$ (see Fig. 5 from ref. [44]).
c. Regional biomass-burning conditions: days with average AAE and SAE satisfying $1.5 \leq \text{AAE} \leq 3.5$ and $\text{SAE} \geq 1.5$ (see Fig. 5 from ref. [44]).

4. Results and Discussions

4.1. Characterization of aerosol physical properties under the selected conditions

Figure 4 presents the AOD and AAOD time series at 440 nm from February 2016 to April 2024 at the ATTO site. The data reveal a seasonal pattern, which can be interpreted by observing that the dry season corresponds to the period with a marked increase in aerosol emissions, as shown by the AOD peaks in the time series. Conversely, the wet season shows minimal aerosol loading, represented by consistently lower AOD and AAOD values. It is worth mentioning that this pattern occurs in all years and is very well characterized in the literature [29].

In the wet season, the average and standard error values for AOD and AAOD were, respectively, 0.124(8) and 0.0062(8), reflecting the clean atmospheric conditions typical of this period. High precipitation rates contribute significantly to atmospheric cleansing, as raindrops capture and remove aerosol particles through wet deposition. This seasonal cycle is consistent with known patterns of aerosol optical properties in the Amazon Basin [28, 44].

Conversely, the dry season is characterized by markedly higher AOD and AAOD average values of 0.32(1) and 0.0191(9), respectively. This period coincides with increased biomass-burning activities, emitting large amounts of aerosols. This high aerosol loading can significantly influence the regional radiation budget [62], impacting climate and weather patterns. The peaks in AOD during the dry season are primarily attributable to biomass burning. However, an important fraction of black carbon (∼30%) comes from long-range transport plumes originating from the western African continent [30]. Fires release a mix of organic particles and black carbon, which are highly effective at scattering and absorbing solar radiation, as evidenced by the AOD and AAOD peak correlation.

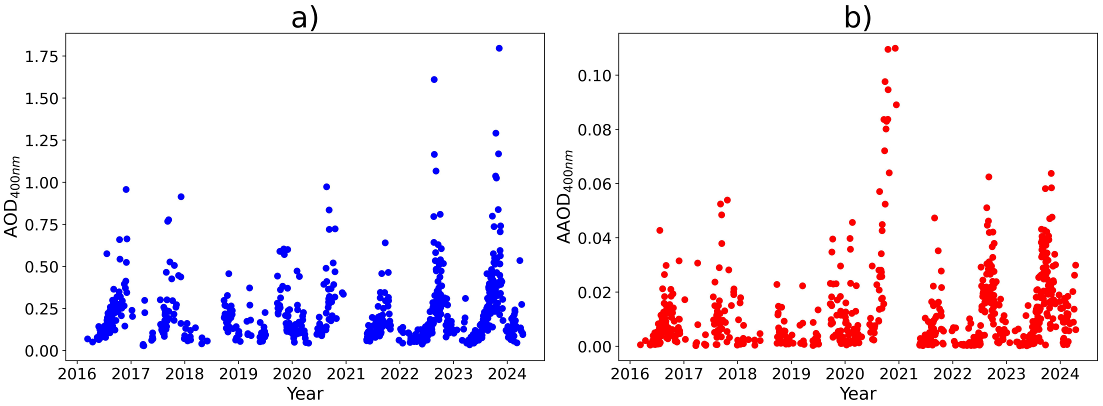

Figure 4: Time series of (a) aerosol optical depth (AOD) and (b) absorption AOD (AAOD) measured at 440 nm from 2016 to 2024 at the ATTO site. Please note the different y-axis.

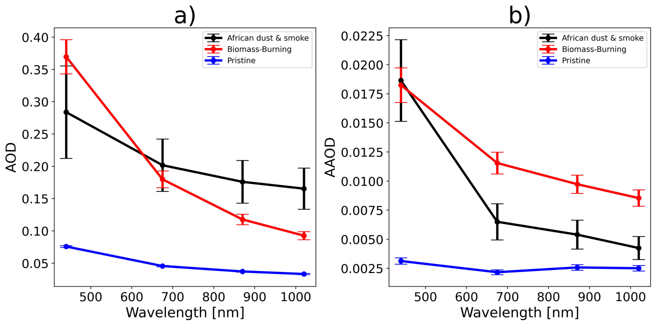

Figure 5: Wavelength-dependency of (a) aerosol optical depth (AOD) and (b) absorption AOD (AAOD). The quantities were obtained with data from 2016 to 2024. Each color represents a different atmospheric condition. The error bars are the standard error, defined as $\sigma_E = \sigma/\sqrt{\mathrm{N}}$, where σ is the standard-deviation and N is the number of observations. Please note the different y-axis.

Figure 5(a) illustrates the AOD as a function of wavelength for the three distinct atmospheric conditions: African dust and smoke, biomass burning, and pristine conditions. The average AOD at 440 nm is highest under biomass burning conditions (0.37), followed by African dust and smoke conditions (0.28) and pristine conditions (0.07). This indicates that the aerosol loading in the atmosphere is greater during the biomass burning period and when there is intrusion of African dust and smoke, resulting in greater extinction of solar radiation. The spectral dependency of AOD also differs between atmospheric conditions, reflecting the different particle chemical compositions and size distributions.

Under biomass burning conditions, the AOD exhibits a more pronounced decrease with wavelength, ranging from 0.37 at 440 nm to 0.09 at 1020 nm. This steeper spectral dependency indicates that the aerosol population was dominated by particles with sizes comparable to the shorter wavelengths of the visible spectrum, with high scattering efficiencies. In fact, biomass burning emissions typically generate fine-mode particles (radius $< 0.5\ \mu m$), effectively scattering light at shorter wavelengths. Figure 6 shows the aerosol volume size distribution with a predominance of fine mode particles under biomass burning conditions, corroborating this result. Figure 6 shows that the aerosol populations differ significantly during the three selected conditions. For biomass-burning conditions, the peak in $dV/d\ln r$, where V and r are the aerosol volume and radius, respectively, is at 148 nm, of 0.039(3) $\mu\text{m}^3/\mu\text{m}^2$. This fine mode peak is much more pronounced compared to the African and pristine conditions of 0.018(9) and 0.0053(2) $\mu\text{m}^3/\mu\text{m}^2$, respectively, at 148 and 113 nm, respectively.

On the other hand, under African dust and smoke conditions, the variation of AOD with wavelength is less pronounced, ranging from 0.28 at 440 nm to 0.17 at 1020 nm. This implies that the aerosol particles

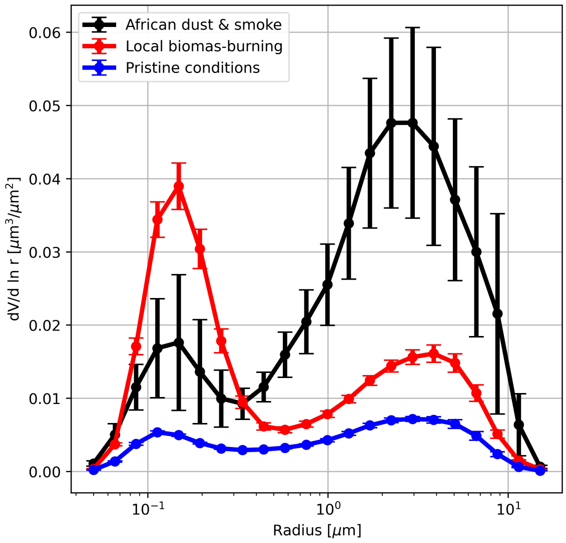

Figure 6: Average aerosol volume size distributions for the three selected periods obtained with data from 2016 to 2024. The x-scale is logarithmic. The error bars are the standard error, defined as $\sigma_E = \sigma/\sqrt{\mathrm{N}}$, where σ is the standard-deviation and N is the number of measurements.

are larger, a typical characteristic of mineral dust transported over long distances. Larger particles affect solar radiation more uniformly over a wider range of wavelengths, resulting in an AOD curve that decreases less steeply with wavelength. This is also corroborated by Figure 6, which shows a strong peak of 0.048(10) $\mu\text{m}^3/\mu\text{m}^2$ at about 2.9 μm in $dV/d\ln r$ for the African conditions at the aerosol coarse mode. In contrast, biomass-burning and pristine conditions presented, at 3.9 and 2.9 μm, respectively, peaks of 0.016(1) and 0.0072(3) $\mu\text{m}^3/\mu\text{m}^2$, respectively. In addition, under pristine conditions, the AOD is very low and nearly constant across wavelengths, indicating a relatively clean atmosphere with a minimal concentration of aerosols. It is worth noting that although almost constant, the AOD decreases from 0.076(1) to 0.033(1), which indicates that natural aerosols are more efficient in scattering radiation at shorter wavelengths closer to the UV region.

Figure 5(b) shows the AAOD as a function of wavelength for the same atmospheric conditions. Similarly to AOD, the AAOD is highest in biomass burning periods, followed by African dust and smoke conditions, and is lowest under pristine conditions. During the biomass burning period, the AAOD is particularly high above 700 nm, consistent with the higher concentration of fine mode aerosols (Figure 6) and the absorption efficiency of carbonaceous aerosols emitted from wildfires. It is worth noting that the average AAOD at 440 nm for biomass-burning and African advection periods is the same (0.019), likely due to the presence of carbonaceous particles in both scenarios that strongly absorb radiation at shorter wavelengths. That leads to a steeper spectral dependency for AAOD during African advection conditions due to the presence of mineral dust aerosols, which affect the absorption efficiency differently across the spectrum. On the other hand, the smaller and more homogeneous carbonaceous particles from regional biomass burning showed more uniform absorption spectra.

The AAOD is significantly lower across all wavelengths under pristine conditions, consistent with the lower aerosol concentrations presented in Figure 6. The AAOD remains nearly constant across the spectrum, suggesting that the particles present are from local sources, such as biogenic ones or secondary organic aerosols, which do not have strong wavelength-dependent absorption characteristics compared to the other aerosol conditions. However, it is important to note that from 675 to 1020 nm, the AAOD increases slightly from 0.0022(2) to 0.0025(2), respectively. This behavior, the opposite of the trend observed in other atmospheric conditions, indicates that natural aerosols (most likely secondary organic aerosols) may also efficiently absorb radiation in the visible red to near-infrared electromagnetic range. The constancy and low values of AAOD in pristine conditions imply that the atmosphere is relatively clean, with minimal contributions from anthropogenic or large-scale natural events such as atmospheric plumes of dust or wildfires.

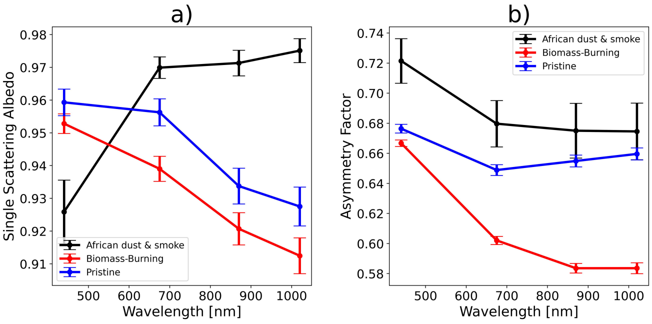

Figure 7: Wavelength-dependency of the (a) single scattering albedo and (b) the asymmetry factor. Each color represents a different atmospheric condition. The error bars are the standard error, defined as $\sigma_E = \sigma/\sqrt{\mathrm{N}}$, where σ is the standard-deviation and N is the number of measurements. Please note the different y-axis.

Figure 7(a) and (b) highlight the SSA and AF spectral behavior, respectively. The SSA values are high across all wavelengths, ranging from approximately 0.91 to 0.98, indicating scattering dominance, also highlighted by the positive AF values. Biomass-burning aerosols show overall the lowest SSA, decreasing from about 0.95 at 440 nm to $\sim$ 0.91 at 1020 nm, highlighting significant absorption by carbonaceous particles like black carbon. In contrast, African dust and smoke aerosol conditions have the lowest SSA at 440 nm, of about 0.93.This indicates a significant contribution from both dust and brown carbon aerosols, which dominate absorption in the near-ultraviolet region [63]. Pristine conditions exhibit the highest SSA at 440 nm, reaching 0.98, but it decreases to approximately 0.93 at 1020 nm. This trend is likely attributed to secondary aerosols formed from oxidized isoprene, which may absorb radiation in the visible and near-infrared regions [31].

The AF shown in Figure 7(b) reflects the directional scattering properties of light by the different aerosol conditions. African dust and smoke exhibit the highest asymmetry values (AF $>$ 0.68) across all wavelengths, indicating substantial forward scattering typical of larger particles. Biomass-burning aerosols show a significant decrease in the asymmetry factor with increasing wavelength, suggesting less directional scattering for smaller particles. As shown in Figure 6, biomass-burning aerosols are dominated by fine particles (submicron size). These smaller particles are more efficient at scattering shorter wavelengths but scatter light less directionally as the wavelength increases, leading to the observed decrease in AF. Under pristine conditions, the asymmetry factor is relatively stable and shows the lowest values (AF $\approx$ 0.65), reflecting more isotropic scattering, typical of smaller or natural particles. These patterns on SSA and AF emphasize the dominant role of forward scattering for all aerosol types, with important implications for Earth's radiative balance and climate processes.

4.2. Wavelength-dependency of the aerosol refractive indices

Figure 8 illustrates the wavelength dependence of the imaginary and real parts of the refractive index for aerosols under the three selected atmospheric conditions. As shown in Equation (18), the imaginary and real parts of the refractive index are directly related to the absorptive and scattering properties of the aerosols, respectively, providing insights into how different aerosol types interact with solar radiation. Figure 8(a) shows that, for biomass burning conditions, the imaginary part of the refractive index increases with wavelength, from 0.008(1) to 0.009(1) at 440 and 1020 nm, respectively. In contrast, the real component decreases from 1.507(4) to 1.491(5) at 440 and 1020 nm, respectively. These trends indicate that this particular aerosol population rich in black carbon and organic compounds absorbs radiation more effectively at longer wavelengths (e.g., red and near-infrared) and less at smaller ones (e.g., UV). In contrast, the real component decreases with increasing wavelength. This behavior is typical of carbonaceous particles in the infrared region, such as the black and brown carbon components [57, 64]. In particular, [65] shows that for the wavelengths in the UV and visible range, brown carbon dominates the absorption, which ceases at about 660 nm, while black carbon dominates the absorption afterward. The literature also corroborates these results.

If we consider exclusively the core of a pure black carbon aerosol, its refractive index is $1.67 + 0.67i$ [66]. However, in the atmosphere, biomass-burning aerosols are aged and oxidized, which adds a coating to the particles, changing their optical properties. For example, [67] have shown that biomass-burning oxygenated aerosols (BBOA) have a real refractive index at 520 nm ranging from 1.47 to 1.64 and an imaginary part ranging from less than 0.01 to about 0.04. According to the authors, this strong variability in both real and imaginary parts depends mainly on the combustion efficiency and particle age.

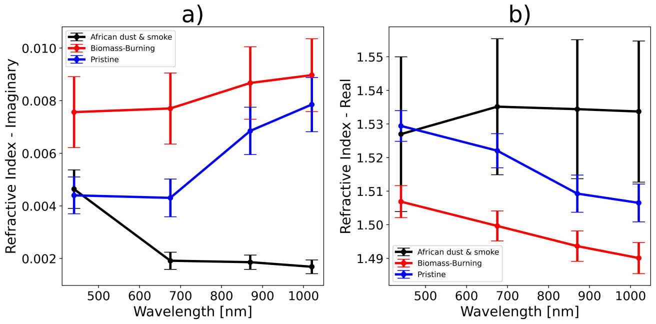

Figure 8: Wavelength-dependency of the (a) imaginary and (b) real components of the refractive index. Each color represents a different atmospheric condition. The error bars are the standard error, defined as $\sigma_E = \sigma/\sqrt{\text{N}}$, where σ is the standard-deviation and N is the number of measurements. Please note the different y-axis.

Under African dust and smoke conditions, the real part of the refractive index shows an initial small increase with wavelength from 440 nm up to 675 nm, from 1.523(23) to 1.535(20), followed by a neglectable decrease, remaining roughly constant up to 1020 nm. In contrast, the imaginary part strongly decreases from 0.0046(7) at 440 nm to 0.0019(3) at 675 nm and then remains roughly constant up to 1020 nm. This behavior suggests mineral dust particles absorb more efficiently in the UV-visible spectrum. The presence of such minerals in African dust can lead to enhanced absorption at these wavelengths, distinguishing it from biomass-burning aerosols. For example, a similar behavior, particularly for the imaginary part, was obtained for Saharan dust at the UV-visible range [68]. From 305 to 955 nm, the imaginary component of the refractive index varied from 0.05 to 0.003, which agrees with what has been observed for the ATTO site, especially considering that this particular aerosol population aged about 14 days from the Saharan region to the central Amazon. In addition, for the real component of the refractive index, it has been considered that dust particles are within the range from 1.48 to 1.56 [69], which also agrees with what has been observed for the ATTO site.

Under pristine conditions, the imaginary part remains constant from 440 to 660 nm, of 0.0044(7), increasing afterward to 0.008(1) at 1020 nm. On the other hand, the real part of the refractive index decreases with the wavelength increase from 1.529(5) at 440 nm to 1.507(6) at 1020 nm. This indicates that the biogenic aerosols are relatively efficient in absorbing radiation in the red-infrared range, which agrees with the increase in the AAOD and decreases in the AOD for the same spectral range. It is worth mentioning that most of the fine mode biogenic aerosols in central Amazon are secondary organic aerosols produced by the oxidation of the volatile organic compound isoprene, emitted by the vegetation [29]. It has been observed that the imaginary part of the refractive index of isoprene-oxidized aerosols depends strongly on the oxidation process. A previous study had shown that the imaginary part at 375 nm varied from 0.012 for aerosols formed in the presence of ozone and SO_2 to virtually zero when other chemical compounds were involved in the oxidation process [70].

A notable characteristic of these pure isoprene-formed aerosols is that the imaginary part decreases as the wavelength increases, becoming negligible at 800 nm. In contrast, the real part shows some variability, ranging from 1.474(12) at 375 nm to 1.411(29) at 781 nm. However, this variability is less pronounced than that observed for the imaginary part. The differences observed between the refractive indices for pure aerosols derived from isoprene oxidation products and those found in pristine environments in the Amazon are also due to contributions from primary, biogenic particles, whose contrast certainly changes the aerosols' optical properties. In practice, obtaining an average refractive index for the Amazon's primary biogenic components of aerosols is highly complex [1]. This complexity arises from the dependence on numerous factors, including meteorological conditions, availability of solar radiation, and seasonal variations. These factors influence the various sources and emissions of particles, making it challenging to determine a consistent average refractive index. This is an important open question for future Amazonian studies.

Therefore, the distinct spectral behaviors of the imaginary part of the refractive index under these different conditions highlight the diverse optical properties of aerosols from various sources. Biomass-burning aerosols, with their strong absorption in the UV and visible regions, contrast sharply with the mineral dust aerosols from African conditions, which show enhanced absorption in the visible red to near-infrared regions. Pristine conditions, with their characteristic absorption pattern, further underscore the contrast between natural and pollution-influenced aerosol properties.

5. Conclusions

This paper applies the concept of refractive index to atmospheric aerosols treated as a dielectric medium. It examines changes in the refractive index and other critical aerosol optical properties under different atmospheric conditions in the central Amazon, using data from the AERONET network. By analyzing data collected during natural Amazonian conditions, regional biomass-burning events, and African dust and smoke advection, we provided a comprehensive view of how different aerosol sources impact the real and imaginary components of the refractive index. The study presents a well-known physical characterization of aerosol optical properties, where distinct seasonal patterns are observed. Higher AOD and AAOD were observed during the dry season due to biomass burning. In particular, the biomass-burning conditions were associated with the dominance of fine particles, leading to a greater influence on radiation scattering, especially at shorter wavelengths. During the wet season, characterized by the prevalence of periods of pristine conditions, lower values of AOD and AAOD were observed, reflecting the clean atmospheric state typical of this period. In contrast, periods influenced by African dust and smoke advection exhibited larger aerosol particles, affecting solar radiation more distinctly across a range of wavelengths.

Our analysis showed distinct wavelength dependencies of the aerosol-intensive properties, such as SSA, AF, and the refractive indices under different atmospheric conditions. Particularly for the refractive index and biomass-burning aerosols, the imaginary part of the refractive index increased with wavelength, indicating enhanced absorption at longer wavelengths, typical of carbonaceous particles. Conversely, the real part decreased with wavelength, highlighting their important and not negligible scattering properties. Under pristine conditions, biogenic aerosols efficiently absorb red-infrared radiation, with the imaginary part of the refractive index increasing at longer wavelengths and the real part decreasing. This behavior is likely influenced by the oxidation of isoprene from vegetation. For African dust and smoke conditions, the real part of the refractive index initially increased with wavelength up to 675 nm before stabilizing, while the imaginary part decreased significantly. This behavior suggests that mineral dust particles from Africa absorb more efficiently in the UV-visible spectrum, distinguishing them from biomass-burning aerosols. This distinction highlights the unique optical properties of different aerosol types and their varied interactions with solar radiation.

The characteristic seasonal aerosol behaviors in the Amazon have important implications for climate modeling and environmental assessments. The results discussed in this study can improve the representation of aerosol radiative effects in climate models, particularly for tropical regions, where aerosol sources and seasonal variability are highly dynamic. Thus, understanding these behaviors is crucial for assessing radiative forcing and developing strategies to mitigate the impacts of climate change. In addition, incorporating AERONET data into the theoretical frameworks of electromagnetism courses can potentially enhance the pedagogical effectiveness of physics and environmental education. Students gain practical insights into the complex interactions between aerosols and electromagnetic radiation, bridging the gap between theoretical knowledge and real-world applications. This interdisciplinary approach enriches the learning experience and fosters a deeper understanding of atmospheric science and its implications for climate and environmental studies.

Acknowledgments

MAF acknowledges the Conselho Nacional de Desenvolvimento Científico e Tecnológico (CNPq), project number 407752/2023-4. PHTT acknowledges the Fundação de Amparo à Pesquisa do Estado de São Paulo (FAPESP), grant 2023/15954-1. LVR acknowledges the CNPq, project number 304819/2022–0. PA acknowledges support from FAPESP, grant 2023/04358-9, and CNPq, project number 440012/2024-4.

Data availability

All data obtained from the AERONET network and Python codes used in this study are available at https://github.com/marcomac27/paper_AERONET_RI.

References

[1] J.H. Seinfeld and S.N. Pandis, *Atmospheric chemistry and physics: from air pollution to climate change* (John Wiley & Sons, New Jersey, 2016)

[2] J.M. Wallace and P.V. Hobbs, *Atmospheric science: an introductory survey* (Elsevier, Amsterdam, 2006).

[3] C.F. Bohren and D.R. Huffman, *Absorption and Scattering of Light by Small Particles* (John Wiley & Sons, New Jersey, 2008).

[4] C. Tebaldi, K. Debeire, V. Eyring, E. Fischer, J. Fyfe, P. Friedlingstein, R. Knutti, J. Lowe, B. O'Neill, B. Sanderson et al., Earth System Dynamics **12**, 253 (2021).

[5] A. Pirani, J.S. Fuglestvedt, E. Byers, B. O'Neill, K. Riahi, J.Y. Lee, J. Marotzke, S.K. Rose, R. Schaeffer and C. Tebaldi, npj Climate Action **3**, 1 (2024).

[6] R.P. Allan, P.A. Arias, S. Berger, J.G. Canadell, C. Cassou, D. Chen, A. Cherchi, S.L. Connors, E. Coppola, F.A. Cruz et al., in: *Climate Change 2021: The Physical Science Basis. Contribution of Working Group I to the Sixth Assessment Report of the Intergovernmental Panel on Climate Change* (Cambridge University Press, Cambridge, 2023).

[7] U. Lohmann and J. Feichter, Atmos. Chem. Phys. **5**, 715 (2005).

[8] R. Burnett, H. Chen, M. Szyszkowicz, N. Fann, B. Hubbell, C.A. Pope III, J.S. Apte, M. Brauer, A. Cohen, S. Weichenthal et al., Proceedings of the National Academy of Sciences **115**, 9592 (2018).

[9] V.A. Southerland, M. Brauer, A. Mohegh, M.S. Hammer, A. Van Donkelaar, R.V. Martin, J.S. Apte and S.C. Anenberg, The Lancet Planetary Health **6**, e139 (2022).

[10] D.M. Westervelt, L.W. Horowitz, V. Naik, J.C. Golaz and D.L. Mauzerall, Atmos. Chem. Phys. **15**, 12681 (2015).

[11] K.R. Smith, H. Frumkin, K. Balakrishnan, C.D. Butler, Z.A. Chafe, I. Fairlie, P. Kinney, T. Kjellstrom, D.L. Mauzerall, T.E. McKone et al., Energy and human health, Annual Review of Public Health **34**, 159 (2013).

[12] D. Shindell, J.C.I. Kuylenstierna, E. Vignati, R. van Dingenen, M. Amann, Z. Klimont, S.C. Anenberg, N. Muller, G. Janssens-Maenhout, F. Raes et al., Science **335**, 183 (2012).

[13] J. Rogelj, D.T. Shindell, K. Jiang, S. Fifita, V. Ginzburg, C. Handa, H.S. Kheshgi, S. Kobayashi, E. Kriegler, L. Mundaca et al., *Global Warming of 1.5°C, IPCC Special Report* (Intergovernmental Panel on Climate Change, Geneva, 2018).

[14] J.R. Reitz, *Foundations of electromagnetic theory* (Pearson Education, Tamil Nadu, 2009).

[15] H.L. Green and W.R. Lane, *Particulate Clouds: Dusts, Smokes and Mists. Their Physics and Physical Chemistry and Industrial and Environmental Aspects* (Academic Press, London, 1957).

[16] R. Whytlaw-Gray and H.S. Patterson, Nature **130**, 260 (1932).

[17] G.M. Hidy, Aerosol Science and Engineering **3**, 1 (2019).

[18] L. Rayleigh, Phil. Mag. **41**, 274 (1871).

[19] L. Lorenz, Det Kongelige Danske Videnskabernes Selskabs Skrifter **1**, 1 (1890).

[20] A. Ångström, Geografiska Annaler **11**, 156 (1929).

[21] A. Ångström, Geografiska Annaler **12**, 130 (1930).

[22] G. Mie, Ann. Phys. (Leipzig) **330**, 377 (1908).

[23] D. Sinclair and V.K. La Mer, Chemical Reviews **44**, 245 (1949).

[24] F. Volz, Arch. Meteorol. Geophys. Bioklim. B **10**, 100 (1959).

[25] B.N. Holben, T.F. Eck, I. Slutsker, D. Tanré, J.P. Buis, A. Setzer, E. Vermote, J.A. Reagan, Y.J. Kaufman, T. Nakajima et al., Remote Sensing of Environment **66**, 1 (1998).

[26] O. Dubovik and M.D. King, J. Geophys. Res.: Atmos. **105**, 20673 (2000).

[27] A. Smirhov, B.N. Holben, M.D. King, Y.J. Kaufman, T.F. Eck and I. Slutsker, J. Geophys. Res. **105**, 9791 (2000).

[28] R.S. Palácios, K.S. Romera, L.F.A. Curado, N.M. Banga, L.D. Rothmund, F.S. Sallo, D. Morais, A.C.A. Santos, T.J. Moraes and F.G. Morais, Aerosol and Air Quality Res. **20**, 139 (2020).

[29] P. Artaxo, H.C. Hansson, M.O. Andreae, J. Bäck, E. Gomes-Alves, H.M.J. Barbosa, F. Bender, E. Bourtsoukidis, S. Carbone, J. Chi et al., Tellus B: Chem. Phys. Meteorol. **24**, 24 (2022).

[30] B.A. Holanda, M.A. Franco, D. Walter, P. Artaxo, S. Carbone, Y. Cheng, S. Chowdhury, F. Ditas, M. Gysel-Beer, T. Klimach et al., Commun. Earth Environ. **4**, 154 (2023).

[31] M.A. Franco, F.G. Morais, L.V. Rizzo, R. Palácios, R. Valiati, M. Teixeira, L.A.T. Machado and P. Artaxo, Meteorol. Atmos. Phys. **136**, 15 (2024).

[32] O. Boucher, *Atmospheric aerosols* (Springer, New York, 2015).

[33] M.A. Yamasoe and M.P. Corrêa, *Processos Radiativos na Atmosfera* (Oficina de Textos, São Paulo, 2016).

[34] M.O. Andreae and A. Gelencsér, Atmos. Chem. Phys. **6**, 3131 (2006).

[35] T.C. Bond, S.J. Doherty, D.W. Fahey, P.M. Forster, T. Berntsen, B.J. DeAngelo, M.G. Flanner, S. Ghan, B. Kärcher, D. Koch et al., J. Geophys. Res.: Atmos. **118**, 5380 (2013).

[36] Q. Zhang, D. Lu, X. Yang, P. Zuo, H. Yang, Q. Fu, Q. Liu and G. Jiang, Environ. Sci. Technol. **54**, 9274 (2020).

[37] H.D. Goodfellow and E.F. Curd, *Physical fundamentals* (Academic Press, Massachusetts, 2020).

[38] D.M. Giles, A. Sinyuk, M.G. Sorokin, J.S. Schafer, A. Smirnov, I. Slutsker, T.F. Eck, B.N. Holben, J.R. Lewis, E.J. Campbell et al., Atmos. Meas. Tech. **12**, 169 (2019).

[39] M.N. Polyanskiy, Sci. Data **11**, 94 (2024).

[40] D.J. Griffiths, *Introduction to Electrodynamics* (Cambridge University Press, Cambridge, 2023).

[41] J.D. Jackson, *Classical Electrodynamics* (John Wiley & Sons, New Jersey, 2012).

[42] AERONET, *AERONET Inversion Products (Version 3)*, available in: https://aeronet.gsfc.nasa.gov/new_web/Documents/Inversion_products_for_V3.pdf, accessed in: 27/04/2024.

[43] H. Horvath, Journal of Quantitative Spectroscopy and Radiative Transfer **110**, 787 (2009).

[44] F.G. Morais, M.A. Franco, R. Palácios, L.A.T. Machado, L.V. Rizzo, H.M.J. Barbosa, F. Jorge, J.S. Schafer, B.N. Holben, E. Landulfo et al., Atmosphere **13**, 1328 (2022).

[45] R.C. Levy, L.A. Remer, S. Mattoo, E.F. Vermote and Y.J. Kaufman, Journal of Geophysical Research: Atmospheres **112**, 1 (2007).

[46] D.J. Diner, J.C. Beckert, T.H. Reilly, C.J. Bruegge, J.E. Conel, R.A. Kahn, J.V. Martonchik, T.P. Ackerman, R. Davies, S.A.W. Gerstl et al., IEEE Transactions on Geoscience and Remote Sensing **36**, 1072 (1998).

[47] M.O. Andreae, O.C. Acevedo, A. Araújo, P. Artaxo, C.G.G. Barbosa, H.M.J. Barbosa, J. Brito, S. Carbone, X. Chi, B.B.L. Cintra, et al., Atmos. Chem. Phys. **15**, 10723 (2015).

[48] C. Pöhlker, D. Walter, H. Paulsen, T. Könemann, E. Rodríguez-Caballero, D. Moran-Zuloaga, J. Brito, S. Carbone, C. Degrendele, V.R. Despré et al., Atmos. Chem. Phys. **19**, 8425 (2019).

[49] L.A.T. Machado, M.A. Franco, L.A. Kremper, F. Ditas, M.O. Andreae, P. Artaxo, M.A. Cecchini, B.A. Holanda, M.L. Pöhlker, I. Saraiva et al., Atmos. Chem. Phys. **21**, 18065 (2021).

[50] M.A. Franco, F. Ditas, L.A. Kremper, L.A.T. Machado, M.O. Andreae, A. Araújo, H.M.J. Barbosa, J.F. Brito, S. Carbone, B.A. Holanda et al., Atmos. Chem. Phys. **22**, 3469 (2022).

[51] D. Moran-Zuloaga, F. Ditas, D. Walter, J. Saturno, J. Brito, S. Carbone, X. Chi, I.H. Angelis, H. Baars, R.H.M. Godoi, et al., Atmos. Chem. Phys. **18**, 10055 (2018).

[52] M.L. Pöhlker, C. Pöhlker, F. Ditas, T. Klimach, I.H. Angelis, A. Araújo, J. Brito, S. Carbone, Y. Cheng, X. Chi et al., Atmos. Chem. Phys. **16**, 15709 (2016).

[53] M. Prass, M.O. Andreae, A.C. Araújo, P. Artaxo, F. Ditas, W. Elbert, J.D. Förster, M.A. Franco, I.H. Angelis, J. Kesselmeier et al., Biogeosciences **18**, 4873 (2021).

[54] M.A. Franco, R. Valiati, B.A. Holanda, B.B. Meller, L.A. Kremper, L.V. Rizzo, S. Carbone, F.G. Morais, J.P. Nascimento, M.O. Andreae et al., EGUsphere **2024**, 1 (2024).

[55] L. Wu, X. Li, H. Kim, H. Geng, R.H.M. Godoi, C.G.G. Barbosa, A.F.L. Godoi, C.I. Yamamoto, R.A.F. Souza, C. Pöhlker et al., Atmos. Chem. Phys. **19**, 1221 (2019).

[56] J. Saturno, B.A. Holanda, C. Pöhlker, F. Ditas, Q. Wang, D. Moran-Zuloaga, J. Brito, S. Carbone, Y. Cheng, X. Ch et al., Atmos. Chem. Phys. **18**, 12817 (2018).

[57] T.C. Bond and R.W. Bergstrom, Aerosol Sci. Technol. **40**, 27 (2006).

[58] B.A. Holanda, M.L. Pöhlker, D. Walter, J. Saturno, M. Sörgel, J. Ditas, F. Ditas, C. Schulz, M.A. Franco, Q. Wang et al., Atmos. Chem. Phys. **20**, 4757 (2020).

[59] A. Cazorla, R. Bahadur, K.J. Suski, J.F. Cahill, D. Chand, B. Schmid, V. Ramanathan and K.A. Prather, Atmos. Chem. Phys. **13**, 9337 (2013).

[60] G.G. Cirino, R.A.F. Souza, D.K. Adams and P. Artaxo, Atmos. Chem. Phys. **14**, 6523 (2014).

[61] R. Palácios, D. Castagna, L. Barbosa, A.P. Souza, B. Imbiriba, C.A. Zolin, D. Nassarden, L. Duarte, F.G. Morais, M.A. Franco et al., Environ. Res. **2024**, 118516 (2024).

[62] E.T. Sena, P. Artaxo and A.L. Correia, Atmos. Chem. Phys. **13**, 1261 (2013).

[63] D.A. Lack and J.M. Langridge, Atmospheric Chemistry and Physics **13**, 10535 (2013).

[64] S. Sonwani, A. Yadav and P. Saxena, Management of contaminants of emerging concern (CEC) in environment **1**, 225 (2021).

[65] D.A. Lack and J.M. Langridge, Atmos. Chem. Phys. **13**, 10535 (2013).

[66] G. Zhao, F. Li and C. Zhao, Atmos. Environ. **240**, 117800 (2020).

[67] B. Luo, Y. Kuang, S. Huang, Q. Song, W. Hu, W. Li, Y. Peng, D. Chen, D. Yue, B. Yuan et al., Atmos. Chem. Phys. **22**, 12401 (2022).

[68] R. Wagner, T. Ajtai, K. Kandler, K. Lieke, C. Linke, T. Müller, M. Schnaiter and M. Vragel, Atmos. Chem. Phys. **12**, 2491 (2012).

[69] O. Dubovik, B.N. Holben, T. Lapyonok, A. Sinyuk, M.I. Mishchenko, P. Yang and I. Slutsker, Geophys. Res. Letters **29**, 54 (2002).

[70] T. Nakayama, K. Sato, T. Imamura and Y. Matsumi, Environ. Sci. Technol. **52**, 2566 (2018).